A direct numerical simulation approach to the study of intrusion fronts

C. HÄRTEL[1], L. KLEISER[1], M. MICHAUD[1] and C.F. STEIN[2]
[1]*Institute of Fluid Dynamics, Swiss Federal Institute of Technology, CH-8092 Zürich, Switzerland*
[2]*Department of Mathematics, Chalmers University of Technology, S-41296 Göteborg, Sweden*

Abstract. A direct numerical simulation approach for the study of gravity currents in a plane channel is described. The numerical method employed is based on a mixed spectral/spectral-element discretization in space together with finite differences in time. For the validation of the code, simulations of Rayleigh–Bénard convection are performed and the results are compared with theoretical predictions and reference data from the literature. The dynamics of gravity currents is then studied by simulations of two-dimensional lock-exchange flow. The results obtained in these simulations are in good agreement with recent experimental data. By a systematic variation of the Grashof number the influence of viscous diffusion on the characteristics of the propagating fronts is assessed.

Key words: gravity currents, lock-exchange flow, direct numerical simulation, spectral method.

1. Introduction

Gravity currents driven by density differences in a fluid are of considerable interest in natural science and engineering (see [1]). Cold-air fronts in the atmosphere, turbidity currents on the ocean floor or powder-snow avalanches are typical examples of gravity currents that can be observed in nature. The study of gravity currents is an important issue in safety engineering and environmental protection, since such currents may form, for example, after an accidental release of dense gases from an industrial plant or the spillage of hydrocarbons on the sea surface. In such situations detailed knowledge about how and where the hazardous substances spread in their environs is needed for both risk assessment and the design of protective measures. In the past numerous theoretical and experimental studies of gravity currents were conducted which aimed at clarifying issues like the inner structure of the currents, their propagation speed or the mixing with ambient fluid [2, 3, 4, 5, 6]. On the other hand, few numerical simulation studies were performed in this field so far, and those which were made employed computational grids which did not allow to capture all small-scale structures of the flow [7, 8]. Direct numerical simulations (DNS) of this problem, where all relevant physical phenomena are thoroughly resolved in space and time, have not been attempted yet.

The present paper reports about the first stage of an ongoing research project in which the DNS approach is applied to study fundamental physical properties of gravity currents. The flow which we consider is the mutual intrusion of two gases of different density in a plane channel. Initially, the two gases are separated by a vertical membrane. After the removal of the membrane, a heavy-gas front and a light-gas front develop and propagate along the lower and the upper channel wall, respectively. A principle sketch of the setup and the resulting flow is provided in Figure 1. This type of flow has been extensively studied in experiments and is often called the lock-exchange problem [1, 9]. In the present stage of our project we focus on the simulation of strictly two-dimensional flows. Simulations of the full three-dimensional
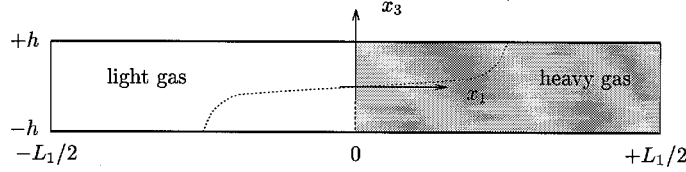
Figure 1. Principle sketch of lock-exchange flow in a channel of length L_1 and height $2h$. The dotted line gives the interface between the two gases some time after the release.

problem are currently being prepared. All simulations are based on the Boussinesq Equations in which density differences are assumed to be small. To solve these equations numerically, we employ a high-order method which will be described in detail.

In the following section we will lay out the governing equations and discuss the dimensionless parameters that enter the problem. The description of the numerical method employed is then given in Section 3. To validate our code, we have conducted simulations of Rayleigh–Bénard convection, and the respective results are given in Section 4. In Section 5 we present the simulations of two-dimensional lock-exchange flow. Finally, in Section 6, a summary of our results, together with some concluding remarks, will be given.

2. Governing equations

Since we are primarily interested in flows with small density differences, we employ the Boussinesq approximations in the budget equations for mass, momentum and energy for the mathematical description of the flow [10]. The variations in density $\tilde{\rho}$ are assumed to be caused by variations in temperature $\tilde{T}$ only (a tilde denotes dimensional flow variables), *i.e.*

$$\frac{\tilde{\rho} - \tilde{\rho}_0}{\tilde{\rho}_0} = \beta(\tilde{T} - \tilde{T}_0). \tag{1}$$

In the above equation $\tilde{\rho}_0$ and $\tilde{T}_0$ denote the reference values of density and temperature, respectively, while β is the heat-expansion coefficient of the fluid.

In the Boussinesq Equations density variations are accounted for only in the buoyancy term in the momentum equation. If the buoyancy force acts in the normal direction x_3 (see Figure 1), these equations take the following dimensionless form

$$\frac{\partial u_k}{\partial x_k} = 0, \tag{2}$$

$$\frac{\partial u_i}{\partial t} + \frac{\partial (u_i u_k)}{\partial x_k} = -\frac{\partial p}{\partial x_i} + \frac{1}{\sqrt{\mathrm{Gr}}} \frac{\partial^2 u_i}{\partial x_k \, \partial x_k} + T\delta_{i3}, \tag{3}$$

$$\frac{\partial T}{\partial t} + \frac{\partial (T u_k)}{\partial x_k} = \frac{1}{\sqrt{\mathrm{GrPr}^2}} \frac{\partial^2 T}{\partial x_k \, \partial x_k}, \tag{4}$$

where u_i denotes the velocity components, p the pressure and T the temperature.

In (2)–(4) all terms have been made dimensionless by the channel half-width h, the temperature difference $\Delta \tilde{T} = \tilde{T}_{\max} - \tilde{T}_{\min}$ and the buoyancy velocity $\tilde{u}_b$

$$\tilde{u}_b = \sqrt{g'h}. \tag{5}$$

In (5) g' denotes the reduced gravity (see [1]) which is computed from the gravitational acceleration g by

$$g' = g\beta\Delta\tilde{T}. \tag{6}$$

The pressure p in (3) has been normalized by $\tilde{\rho}\tilde{u}_b^2$ and the non-dimensional temperature is defined as

$$T = \frac{\tilde{T} - \tilde{T}_{\min}}{\Delta T}. \tag{7}$$

From the normalization two dimensionless parameters arise. The first of these is the Prandtl number Pr

$$\mathrm{Pr} = \frac{\nu}{\kappa}, \tag{8}$$

which is the ratio of kinematic viscosity ν and molecular diffusivity of temperature κ. The second parameter is the ratio of buoyancy forces and viscous forces and is usually referred to as the Grashof number Gr [10]

$$\mathrm{Gr} = \left(\frac{\tilde{u}_b h}{\nu}\right)^2. \tag{9}$$

From the momentum budget (3) one finds that, in the present case of natural convection, the square root of the Grashof number plays the same role as the Reynolds number in forced convection flows. Similarly, $\sqrt{\mathrm{GrPr}^2}$ corresponds to a Péclet number as is seen from Equation (4).

3. Numerical method

The numerical method employed for the integration of the basic equations is an extension of the scheme used in [11] which was developed for the simulation of transition and turbulence in plane channel flow. The computational box is the domain sketched in Figure 1, where the longitudinal and wall-normal direction of the Cartesian coordinate system are denoted by x_1 and x_3, respectively. The third, lateral, direction x_2 has been omitted in the Figure for simplicity.

In the longitudinal direction two diffent types of boundary conditions may be applied: In the lock-exchange simulations the flow is assumed to possess a mirror symmetry with respect to $x_1 = \pm L_1/2$, corresponding to frictionless end walls at these locations. Alternatively, periodic boundary conditions may be applied at $x_1 = \pm L_1/2$. The latter boundary condition is utilized in our computations of Rayleigh–Bénard convection which we chose as the test case for the validation of the code. In the lateral direction x_2 the same types of boundary conditions can be imposed as in x_1, *i.e.* either symmetry or periodicity conditions at $x_2 = \pm L_2/2$. The top and bottom boundaries at $x_3 = \pm 1$ are either rigid no-slip walls or no-stress (*i.e.* free-slip) boundaries, and they may be either isothermal or adiabatic.

3.1. TEMPORAL DISCRETIZATON

The temporal discretization of Equations (3)–(4) is accomplished by a semi-implicit finite-difference method. The diffusive terms and the buoyancy term are discretized by means of a

second-order accurate Crank–Nicolson scheme, while a third-order low-storage Runge–Kutta method is utilized for the nonlinear terms. If we introduce the superscript m to denote the mth Runge–Kutta substep ($m = 0, 1, 2, 3$) within an individual time step $\Delta t = t^{n+1} - t^n$, the time-discretized governing equations read

$$\frac{\partial u_k^{m+1}}{\partial x_k} = 0, \tag{10}$$

$$\frac{\partial^2 u_i^{m+1}}{\partial x_k \, \partial x_k} - \lambda u_i^{m+1} - \frac{\partial q^{m+1}}{\partial x_i} + \sqrt{\mathrm{Gr}}\, T^{m+1}\delta_{i3} = -r_i^m, \tag{11}$$

$$\frac{\partial^2 T^{m+1}}{\partial x_k \, \partial x_k} - \mu T^{m+1} = -r_T^m, \tag{12}$$

where

$$\mu = \frac{2\sqrt{\mathrm{GrPr}^2}}{\Delta^m t}, \qquad \lambda = \frac{2\sqrt{\mathrm{Gr}}}{\Delta^m t} \tag{13}$$

and q is the modified pressure which is defined as

$$q = 2\sqrt{\mathrm{Gr}}\left(\tfrac{1}{2}u_i u_i + p\right). \tag{14}$$

The respective right-hand sides of Equations (11, 12) are

$$r_i^m = 2\sqrt{\mathrm{Gr}}\left[\frac{u_i^m}{\Delta^m t} + \gamma_1 M_i^m + \gamma_2 M_i^{m-1}\right] + \frac{\partial^2 u_i^m}{\partial x_k \, \partial x_k} + \sqrt{\mathrm{Gr}}\, T^m\delta_{i3}, \tag{15}$$

$$r_T^m = 2\sqrt{\mathrm{GrPr}^2}\left[\frac{T^m}{\Delta^m t} + \gamma_1 N^m + \gamma_2 N^{m-1}\right] + \frac{\partial^2 T^m}{\partial x_k \, \partial x_k}, \tag{16}$$

where γ_1 and γ_2 denote the Runge–Kutta coefficients of each substep m [12]. In (15, 16) M_i and N designate the nonlinearities which are treated explicitly

$$M_i = -u_k\left(\frac{\partial u_i}{\partial x_k} - \frac{\partial u_k}{\partial x_i}\right), \tag{17}$$

$$N = -u_k\frac{\partial T}{\partial x_k}. \tag{18}$$

To enforce the continuity constraint (10) at each intermediate time level, a solution of a Poisson Equation for the modified pressure q^{m+1} is required. We obtain this Poisson equation by taking the divergence of the time-discretized momentum budget (11) which yields

$$\frac{\partial^2 q^{m+1}}{\partial x_k \, \partial x_k} = \frac{\partial r_k^m}{\partial x_k} + \sqrt{\mathrm{Gr}}\frac{\partial T^{m+1}}{\partial x_3}. \tag{19}$$

3.2. SPATIAL DISCRETIZATION IN HOMOGENEOUS DIRECTIONS

The assumption of symmetry or periodicity in the longitudinal and lateral directions allows for the application of a Fourier spectral method in x_1 and x_2. In this approach any dependent variable f, say, is expanded in a complex Fourier series

$$f(x_1, x_2, x_3, t) = \sum_{k_1} \sum_{k_2} \hat{f}(k_1, k_2, x_3, t) \, e^{I(k_1 \alpha_1 x_1 + k_2 \alpha_2 x_2)}, \tag{20}$$

where

$$|k_i| < \frac{N_i}{2}, \quad \alpha_i = \frac{2\pi}{L_i}, \quad (i = 1, 2) \tag{21}$$

and

$$I = \sqrt{-1}. \tag{22}$$

In Equation (21) N_i is the number of grid points used in the direction x_i. In the expansion (20) a hat has been used to denote the Fourier coefficients (or Fourier modes) as will generally be done in this paper. We remark that the Fourier expansion simplifies to an expansion of the flow variables in real sine and cosine series, if symmetry conditions are applied at $\pm L_i/2$, which reduces the computational costs significantly.

Introducing the expansion (20) into (10)–(12) and applying the standard Galerkin procedure [13] we are led to a system of five one-dimensional Helmholtz-type equations for the time advancement of each mode (k_1, k_2)

$$(\hat{u}_1^{m+1})'' - (\mathbf{B} + \lambda)\hat{u}_1^{m+1} - I k_1 \alpha_1 \hat{q}^{m+1} = -\hat{r}_1^m, \tag{23}$$

$$(\hat{u}_2^{m+1})'' - (\mathbf{B} + \lambda)\hat{u}_2^{m+1} - I k_2 \alpha_2 \hat{q}^{m+1} = -\hat{r}_2^m, \tag{24}$$

$$(\hat{u}_3^{m+1})'' - (\mathbf{B} + \lambda)\hat{u}_3^{m+1} - (\hat{q}^{m+1})' + \sqrt{\mathrm{Gr}}\,\hat{T}^{m+1} = -\hat{r}_3^m, \tag{25}$$

$$(\hat{q}^{m+1})'' - \mathbf{B}\,q^{m+1} = I(k_1 \alpha_1 \hat{r}_1^m + k_2 \alpha_2 \hat{r}_2^m) + (\hat{r}_3^m)' + \sqrt{\mathrm{Gr}}\,\frac{\partial \hat{T}^{m+1}}{\partial x_3}, \tag{26}$$

$$(\hat{T}^{m+1})'' - (\mathbf{B} + \mu)\hat{T}^{m+1} = -\hat{r}_T^m, \tag{27}$$

which have to be solved under the continuity constraint

$$I(k_1 \alpha_1 \hat{u}_1^{m+1} + k_2 \alpha_2 \hat{u}_2^{m+1}) + (\hat{u}_3^{m+1})' = 0. \tag{28}$$

In the above equations $\mathbf{B} = (k_1 \alpha_1)^2 + (k_2 \alpha_2)^2$ and the prime denotes differentiation with respect to x_3. Further, $\hat{r}_i^m$ and $\hat{r}_T^m$ are the coefficients of the Fourier transforms of (15) and (16), respectively. For the computation of $\hat{r}_i^m$ and $\hat{r}_T^m$, the nonlinearities M_i and N need to be evaluated at the time levels m and $m - 1$, which is done in a pseudo-spectral manner [13]. This involves a forward Fourier transform of the velocity components and the temperature, the computation of the nonlinear products in real space and the backward transform of these

products to wavenumber space. To make sure that the resulting Fourier coefficients $\hat{M}_i$ and $\hat{N}$ are free of aliasing errors, the 3/2-rule is employed [13].

3.3. SPATIAL DISCRETIZATION IN WALL-NORMAL DIRECTION

The discretization of the system (23)–(28) in the wall-normal direction is accomplished by a spectral-element method where the full domain $-1 \leqslant x_3 \leqslant 1$ is divided into n_e subdomains. The kth element of this decomposition covers the subdomain located between the boundaries x_3^{k-1} and x_3^k ($k = 1, \ldots, n_e$). The boundaries of the individual elements can be chosen freely, the only restrictions being that $x_3^{k-1} > x_3^k$ and that x_3^0 and $x_3^{n_e}$ coincide with the global boundaries of the flow domain at $x_3 = +1$ and $x_3 = -1$, respectively.

In each of the elements a spectral collocation technique [13] is employed which is based on an expansion of the dependent variables in Chebyshev polynomials (Legendre polynomials may be applied alternatively). The number n_p of discrete grid points within each element, being the same for all elements, is a free parameter and determines the approximation order of the spatial discretization in x_3. In each element the discrete mesh points $x_{3,j}^k$ ($j = 1, \ldots, n_p$) are obtained from a linear mapping of the Gauss–Lobatto points [13] of the expansion functions onto the physical domain covered by the kth element. For the Chebyshev polynomials this results in a cosine distribution

$$x_{3,j}^k = \frac{x_3^{k-1} + x_3^k}{2} + \zeta_k \cdot \cos\left(\frac{(j-1)\pi}{n_p - 1}\right), \quad j = 1, \ldots, n_p. \tag{29}$$

In (29) the metric coefficient ζ_k accounts for the size of the subdomain k

$$\zeta_k = \frac{x_3^{k-1} - x_3^k}{2}. \tag{30}$$

Note that the n_pth collocation point of element k coincides with the first collocation point of the element $k + 1$. Consequently, the total number N_3 of grid points in the wall-normal direction is

$$N_3 = n_e(n_p - 1) + 1. \tag{31}$$

In the present method all flow variables (*i.e.* the velocity components, the pressure and the temperature) are located at the same grid points.

The application of the collocation method transforms the ordinary differential Equations (23)–(28) into a set of linear algebraic equations for the vectors of the unknowns $\hat{u}_{i,j}, \hat{q}_j$ and $\hat{T}_j$ at the nodal points $x_{3,j}$ ($j = 1, \ldots, N_3$). If we drop the indices of the time discretization for simplicity, these equations read

$$\hat{\operatorname{div}} \hat{u}_{i,j} = 0, \tag{32}$$

$$\mathcal{D}_3^{(2)}\hat{u}_{1,j} - (\mathrm{B} + \lambda)\hat{u}_{1,j} - Ik_1\alpha_1\hat{q}_j = -\hat{r}_{1,j}, \tag{33}$$

$$\mathcal{D}_3^{(2)}\hat{u}_{2,j} - (\mathrm{B} + \lambda)\hat{u}_{2,j} - Ik_2\alpha_2\hat{q}_j = -\hat{r}_{2,j}, \tag{34}$$

$$\mathcal{D}_3^{(2)}\hat{u}_{3,j} - (\mathrm{B} + \lambda)\hat{u}_{3,j} - \mathcal{D}_3\hat{q}_j = -\hat{r}_{3,j} + \sqrt{\mathrm{Gr}}\,\hat{T}_j, \tag{35}$$
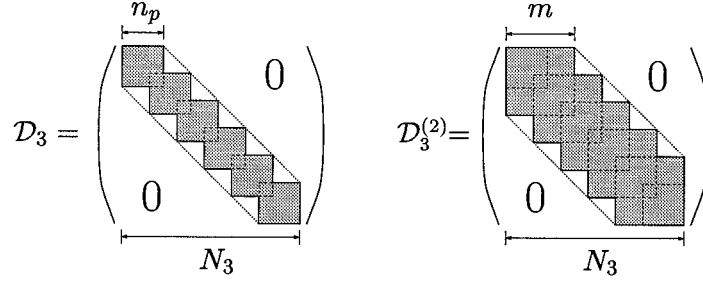
Figure 2. Structure of the differentiation matrices. In the matrix $\mathcal{D}_3$ the blocks overlap by one element. The width m of each block of the matrix $\mathcal{D}_3^{(2)}$ is given by $m = 2n_p - 1$.

$$\mathcal{D}_3^{(2)}\hat{q}_j - \mathbf{B}\,\hat{q}_j = I(k_1\alpha_1\hat{r}_{1,j} + k_2\alpha_2\hat{r}_{2,j}) + \mathcal{D}_3\hat{r}_{3,j} + \sqrt{\mathrm{Gr}}\,\mathcal{D}_3\hat{T}_j, \tag{36}$$

$$\mathcal{D}_3^{(2)}\hat{T}_j - (\mathbf{B} + \mu)\hat{T}_j = -\hat{r}_{T,j}, \tag{37}$$

where the discrete divergence operator in wavenumber space $\hat{\mathrm{div}}$ is given by

$$\hat{\mathrm{div}}\,\hat{u}_{i,j} \equiv I(k_1\alpha_1\hat{u}_{1,j} + k_2\alpha_2\hat{u}_{2,j}) + \mathcal{D}_3\hat{u}_{3,j}, \tag{38}$$

and $\mathcal{D}_3$ and $\mathcal{D}_3^{(2)}$ denote the differentiation matrices of the first and second derivative in the wall-normal direction, respectively. The structure of these differentiation matrices is sketched in Figure 2. The matrix $\mathcal{D}_3$ is composed of n_e individual $n_p \times n_p$ blocks, one block for each of the subdomains. The elements of these blocks are given by the elements of the common $n_p \times n_p$ Chebyshev (or Legendre) differentiation matrix (see [13]) multiplied by the metric coefficient ζ_k given by (30). As a patching condition the solution and its first derivative are required to be continuous across the interface of each two neighboring elements which leads to an overlapping of two adjacent blocks. The matrix element at the position of overlap is then replaced by the arithmetic mean of the respective corner elements of the original $n_p \times n_p$ blocks.

The algorithm employed for the solution of (32)–(37), which will be outlined in the subsequent section, requires that the Poisson equation for the pressure (36) is precisely the discrete divergence of the momentum Equations (33)–(35). This implies that the first and second derivatives in the wall-normal direction have to be consistent in the sense that the application of the operator $\mathcal{D}_3^{(2)}$ is, up to round-off errors, identical with the result of two successive applications of $\mathcal{D}_3$. In other words, the matrix $\mathcal{D}_3^{(2)}$ must be computed from $\mathcal{D}_3$ by

$$\mathcal{D}_3^{(2)} = \mathcal{D}_3^2 \equiv \mathcal{D}_3 \cdot \mathcal{D}_3. \tag{39}$$

Consequently, the matrix $\mathcal{D}_3^{(2)}$ has a bandwidth which is almost double that of $\mathcal{D}_3$. Note that this approach is different from what is usually done in spectral-element methods, since in most approaches the matrix $\mathcal{D}_3^{(2)}$ is constructed analogously to $\mathcal{D}_3$, meaning that $\mathcal{D}_3^{(2)}$ is built up from $n_p \times n_p$ blocks of second-order differentiation matrices derived from the respective expansion functions (see *e.g.* [14, 15]). In that case the matrices of the first and second derivatives are of equal bandwidth.

3.4. SOLUTION OF THE DISCRETIZED SYSTEM

In the discretized system (32)–(37) the solution of the energy equation is decoupled from the solution of the other equations owing to the fact that the convective transport of thermal energy has been discretized explicitly. Equation (37) is therefore solved first. The wall boundary conditions for the temperature equation are either Dirichlet or Neumann conditions, depending on the specific flow problem at hand. In the lock-exchange simulations we use adiabatic walls which corresponds to homogeneous Neumann conditions

$$\frac{\partial T}{\partial x_3} = 0 \quad \text{at} \quad x_3 = \pm 1. \tag{40}$$

On the other hand, isothermal walls are prescribed in the simulations of Rayleigh–Bénard convection, *i.e.*

$$T(x_3 = +1) = 0, \qquad T(x_3 = -1) = 1. \tag{41}$$

Once the temperature field at the new time level is known, it can be inserted into the respective terms of the right-hand sides of Equations (35) and (36). The system (32)–(36) then has to be solved in a coupled manner. For the velocities arbitrary boundary conditions can be prescribed which may be either Dirichlet or Neumann conditions. The only restriction is that the imposed conditions need to be compatible with the continuity equation at the boundaries

$$\hat{\text{div}}\, \hat{u}_{i,j} = 0 \quad \text{at} \quad j = 1, N_3. \tag{42}$$

The difficulty with the coupled solution of (32)–(36) is that the Poisson equation for the pressure cannot readily be solved, since the correct boundary conditions for $\hat{q}_j$ are not known at the outset. Rather they are implicitly determined by (32), *i.e.* the requirement that the discrete divergence of the velocity field $\hat{u}_{i,j}$ has to vanish in the whole domain. The method we employ to solve this problem is an extension of the influence-matrix technique developed by Kleiser and Schumann [16] (see also [13] for a detailed discussion of that scheme). The original algorithm was specifically designed for no-slip walls, while the present version allows for more general boundary conditions at $x_3 = \pm 1$.

In order to derive the desired divergence-free solution for $\hat{u}_{i,j}$, let us consider the general solution of the system (33)–(36) for arbitrary pressure boundary conditions. This general solution can be written as a linear combination of a particular solution $(\hat{u}^p_{i,j}, \hat{q}^p_j)$ with, for example, homogeneous Dirichlet conditions for $\hat{q}_j$, and two solutions $(\hat{u}^{h1}_{i,j}, \hat{q}^{h1}_j)$ and $(\hat{u}^{h2}_{i,j}, \hat{q}^{h2}_j)$ of the associated homogeneous problem, *i.e.* (33)–(36) with zero on the right-hand sides. The pressure boundary conditions of the latter two solutions must be linearly independent and we employ $\hat{q}^{h1}_1 = 0, \hat{q}^{h1}_{N_3} = 1$ and $\hat{q}^{h2}_1 = 1, \hat{q}^{h2}_{N_3} = 0$, respectively. The velocity boundary conditions for the particular solution are the same as those for the full problem; on the other hand, homogeneous velocity boundary conditions have to be imposed for $\hat{u}^{h1}_{i,j}$ and $\hat{u}^{h2}_{i,j}$. These are either Dirichlet or Neumann conditions, depending on the type of boundary conditions used for $\hat{u}_{i,j}$. In terms of the three individual solutions, the general solution $(\hat{u}_{i,j}, \hat{q}_j)$ of the system (33)–(36) can be written as

$$\begin{pmatrix} \hat{u}_{i,j} \\ \hat{q}_j \end{pmatrix} - \begin{pmatrix} \hat{u}^p_{i,j} \\ \hat{q}^p_j \end{pmatrix} + \alpha_1 \begin{pmatrix} \hat{u}^{h1}_{i,j} \\ \hat{q}^{h1}_j \end{pmatrix} + \alpha_2 \begin{pmatrix} \hat{u}^{h2}_{i,j} \\ \hat{q}^{h2}_j \end{pmatrix}, \tag{43}$$

where α_1 and α_2 are yet undetermined coefficients. Note that each pair of boundary conditions for the pressure uniquely determines the pair of coefficients α_1, α_2 and *vice versa*.

The coefficients α_1, α_2 have to be determined such that the resulting velocity field satisfies the continuity constraint. A necessary and sufficient condition for the divergence of the velocity to vanish in the whole domain D is given by (42), *i.e.* by the requirement that it vanish on the boundary ∂D [13, 16]. This condition yields the two linear equations from which the coefficients α_1 and α_2 can be computed

$$\hat{\mathrm{div}}\, \hat{u}_{i,j} = \hat{\mathrm{div}}\, \hat{u}_{i,j}^p + \alpha_1 \hat{\mathrm{div}}\, \hat{u}_{i,j}^{h1} + \alpha_2 \hat{\mathrm{div}}\, \hat{u}_{i,j}^{h2} = 0 \quad \text{at} \quad j = 1, N_3. \tag{44}$$

This is equivalent to

$$\underbrace{\begin{pmatrix} \hat{\mathrm{div}}\, \hat{u}_{i,j}^{h1}(j=1) & \hat{\mathrm{div}}\, \hat{u}_{i,j}^{h2}(j=1) \\ \hat{\mathrm{div}}\, \hat{u}_{i,j}^{h1}(j=N_3) & \hat{\mathrm{div}}\, \hat{u}_{i,j}^{h2}(j=N_3) \end{pmatrix}}_{\text{influence matrix}} \begin{pmatrix} \alpha_1 \\ \alpha_2 \end{pmatrix} = -\begin{pmatrix} \hat{\mathrm{div}}\, \hat{u}_{i,j}^p(j=1) \\ \hat{\mathrm{div}}\, \hat{u}_{i,j}^p(j=N_3) \end{pmatrix}. \tag{45}$$

Inserting the coefficients obtained from (45) into (43) yields the desired divergence-free solution. Note that the homogeneous solutions are independent of the time-dependent right-hand sides of (33)–(36) which allows us to compute and store them prior to the time integration. The same holds for the influence matrix. A pair of homogeneous solutions along with the influence matrix is required for each Fourier mode (k_1, k_2). The only solution that needs to be computed at each time step is the particular solution $(\hat{u}_{i,j}^p, \hat{q}_j^p)$.

If the above procedure is applied, the resulting flow field $\hat{u}_{i,j}$ will not yet be divergence free to machine accuracy. The reason for this is that the discretized momentum budgets (33)–(35) are not fulfilled at $j = 1, N_3$ where the boundary conditions for the velocities are imposed. This fact has to be taken into account in the solution of the discretized Poisson Equation (36), since this equation is the discrete divergence of (33)–(35). An efficient algorithm to correct these additional discretization errors is described in detail in [13].

4. Rayleigh–Bénard convection

For the validation of the code we have performed simulations of two-dimensional Rayleigh–Bénard convection, since for this flow problem extensive reference data are available. From the numerical point of view the only differences between the Rayleigh–Bénard flow and the lock-exchange flow are in the boundary conditions for the temperature (see (40, 41)) and the initial temperature distribution. In the Rayleigh–Bénard problem the walls are assumed to be isothermal and the initial temperature profile is linear

$$T_0 = T(x_1, x_3, t = 0) = \frac{1 - x_3}{2}. \tag{46}$$

The parameter which determines whether or not a convective motion sets in, is the Rayleigh number Ra defined as

$$\mathrm{Ra} = 8 \cdot \mathrm{GrPr}. \tag{47}$$

For higher values of the Rayleigh number the fluid layer becomes unstable and a flow pattern will evolve which is characterized by the system of counter-rotating convection rolls sketched
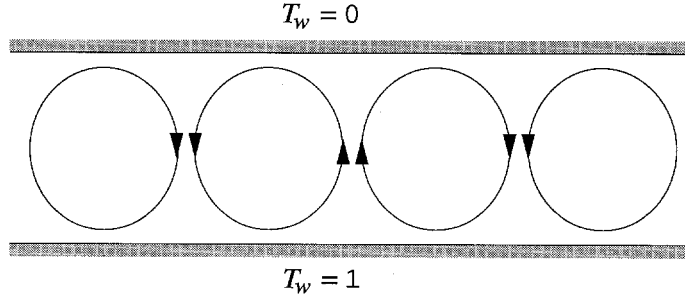
$$T_w = 0$$

Figure 3. Principle sketch of convection rolls in Rayleigh–Bénard flow.

in Figure 3. In the definition (47) a factor of 8 has been included, since the Rayleigh number is commonly based on the full channel height $d = 2h$ as a characteristic length scale [10, 17]. If no-slip conditions are imposed at the lower and upper walls, linear stability theory shows that $Ra_c = 1707 \cdot 76$ is the minimum Rayleigh number for which a convective motion may set in [17]. Ra_c is usually termed the critical Rayleigh number. The associated wavelength α_c of the most unstable eigenmode is $\alpha_c = 2\pi/L_c \approx 1 \cdot 5585$, L_c being the horizontal width of a pair of counter-rotating convection rolls normalized by the channel half-width h.

In all simulations we performed, the length L_1 of the computational domain was set to L_c and the Prandtl number was set to $Pr = 0 \cdot 71$ which is the standard value for air. The Rayleigh numbers of the simulations were all supercritical, but well below the value where a transition to three-dimensional flow patterns can be observed (see [18]). The velocity fields were initialized with fluid at rest. In order to trigger the onset of convection, we disturbed the linear temperature profile (46) by noise of the order of 10^{-10} which was superimposed on the $k_1 = 1$ and $k_1 = 2$ modes. The flow development was then followed in time until a state of steady cellular convection was attained.

An overall impression of the various flow regimes encountered during the temporal evolution of the flow can be gained from the time history of the Fourier modes. For one of the simulations, which we will refer to as SI here, such a time history is given in Figure 4 where the maximum of the Fourier modes of the temperature with respect to x_3 has been plotted

$$\hat{T}_{\max}(k_1, t) = \max_{x_3} |\hat{T}(k_1, x_3, t)|. \tag{48}$$

The Rayleigh number of SI is $Ra = 2400$ and the computational mesh consists of $N_1 \times N_3 = 16 \times 16$ grid points where a single element is used in the wall-normal direction. It is seen from the Figure that the early stage of the flow is governed by an exponential evolution of all modes. Initially, the only mode growing is $k_1 = 1$, while from $t \approx 80$ onwards higher modes start to grow (the initial growth of modes $k_1 \geqslant 5$ is caused by round-off errors). Nonlinear interactions begin to dominate from $t \approx 280$ onwards, eventually leading to a stationary solution which is attained to approximately $t = 320$. From the figure it is seen that in the final stage the amplitude of the highest Fourier mode $k_1 = 7$ is about six orders of magnitude smaller than the amplitude of the lowest mode $k_1 = 1$, which indicates that an excellent numerical resolution is achieved.
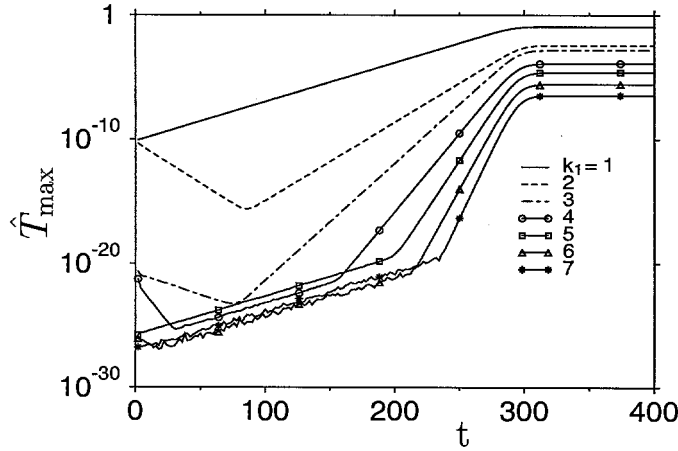
Figure 4. Time history of maximum Fourier modes $\hat{T}_{\max}(k_1)$ of the temperature. Simulation SI of Rayleigh–Bénard convection using 1 element with 16 grid points in the wall-normal direction (Ra = 2400, Pr = 0·71).

Table 1. Amplification rates ω of linear eigenmodes of the Rayleigh–Bénard problem. Comparison of DNS results with linear stability theory (LST). ε_ω denotes the relative error in the DNS results.

	SI $k = 1$	SI $k = 2$	SII $k = 1$	SIII $k = 1$
ω_{LST}	0·072800	−0·15067	0·072800	0·054662
ω_{DNS}	0·072687	−0·15078	0·072686	0·054658
ε_ω	0·16%	0·07%	0·16%	0·015%

4.1. COMPARISON WITH LINEAR STABILITY THEORY

As pointed out before, the initial stage of the flow development is characterized by an exponential evolution of the individual modes, the amplitudes $\hat{T}(t)$ of which develop in time like

$$\frac{|\hat{T}(t)|}{|\hat{T}_0|} = \mathrm{e}^{\omega t} \quad \text{where} \quad \hat{T}_0 = \hat{T}(t = 0). \tag{49}$$

The factor ω in (49) is usually called the amplification rate. Since the initial disturbance amplitudes are small, growth rates and/or decay rates may be compared with the results from a linear stability analysis of the Rayleigh–Bénard problem (see [17]). For the first two modes $k_1 = 1, 2$ of SI such a comparison is provided in Table 1. The results show that the amplification rates obtained from the DNS are in excellent agreement with the theoretical values. The errors in the DNS results are of the order of 0·1%.

In Table 1 results of two other simulations, denoted as SII and SIII, respectively, have been included. Simulation SII differs from SI with respect to the discretization in x_3 only. Three spectral elements of equal size have been used in SII, each of these containing $n_p = 6$ grid points. This results in a total number of $N_3 = 16$ mesh points in the normal direction which is identical to what was used in SI. Table 1 shows that the results of the two simulations are

identical up to six decimal places. The simulations SI and SIII utilize the identical computational mesh, but in SIII no-stress boundary conditions were applied at the walls, rather than no-slip conditions, *i.e.*

$$\partial u_1 / \partial x_3 = 0, \quad \partial u_2 / \partial x_3 = 0, \quad u_3 = 0 \quad \text{at} \quad x_3 = \pm 1, \tag{50}$$

which reads in discretized form

$$\mathcal{D}_3 \hat{u}_{1,j} = 0, \quad \mathcal{D}_3 \hat{u}_{2,j} = 0, \quad \hat{u}_{3,j} = 0 \quad \text{at} \quad j = 1, N_3. \tag{51}$$

For the boundary conditions (50) the fluid layer is more unstable than for no-slip boundaries due to the absence of wall friction. Consequently, convective motions set in at much smaller Rayleigh numbers. The Rayleigh number used in SIII is Ra = 880 which is slightly above the critical Rayleigh number $\mathrm{Ra}_c^* = 657 \cdot 6$ for frictionless boundaries. From Table 1 it is seen that the results of SIII show the same excellent agreement with linear stability theory as do the results of the simulations SI and SII.

4.2. Steady cellular convection

For the highly nonlinear stage of steady cellular convection no theoretical results are available for validation. However, several extensive numerical studies of that flow regime have been conducted in the past, the results of which may be employed for comparison with our DNS. Clever and Busse [18], for example, have analyzed the steady-state equations numerically by means of a Galerkin method. Among other things, they evaluated the average heat flux through the fluid layer which can be expressed in non-dimensional form by the Nusselt number Nu [10]. In our simulations the Nusselt number is given by the average temperature gradient at the wall

$$\mathrm{Nu} = \frac{2}{L_1} \int_{x_1 = -L_1/2}^{L_1/2} \left| \frac{\partial T(x_3 = +1)}{\partial x_3} \right| \, \mathrm{d}x_1. \tag{52}$$

In (52) the factor 2 enters for the same reason as the factor 8 was included in the definition (47) of the Rayleigh number. The results obtained in [18] are summarized in Figure 5 where our present DNS data have been included for comparison. The excellent agreement between the results is readily seen.

5. Lock-exchange flow

5.1. Initialization

In the lock-exchange simulations the flow field is initialized with a fluid at rest, *i.e.* $u_i = 0$ everywhere. In contrast to the straightforward initialization of the temperature field in the Rayleigh–Bénard case, the proper initial values of temperature require more attention in the lock-exchange case. In essence, the initial temperature field consists of a volume of light and heavy gas in the left and right half of the channel, respectively, with some interface of thickness δ in between, *i.e.*

$$T_0(x_1) \equiv T(x_1, x_3, t = 0) = \begin{cases} 1 & \text{for } x_1 \leqslant -\delta/2, \\ 0 & \text{for } x_1 \geqslant \delta/2. \end{cases} \tag{53}$$
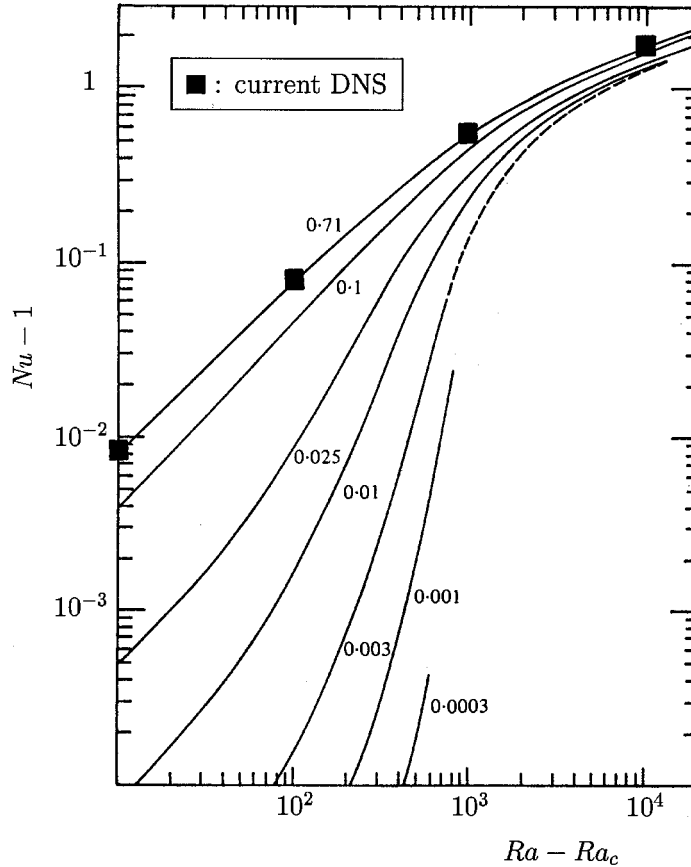
Figure 5. Nusselt number as a function of $Ra - Ra_c$, Ra_c being the critical Rayleigh number. The individual curves give the results for different Prandtl numbers obtained by Clever and Busse [18]. Squares give the present simulation results for $Pr = 0.71$.

In principle δ could be set to zero at the beginning, meaning that the initial temperature distribution is a step function. However, since we use Fourier expansions in x_1, the temperature profile must be continuous and δ has to be finite at $t = 0$. The numerical resolution required in the initial stage depends directly on δ, which makes a careful selection of the interface thickness essential.

To obtain a guess for the initial interface structure, we may consider the case $\delta \approx 0$ at $t = 0$ and compare the relative importance of diffusion and convection of temperature in the start-up phase. Due to the singularity in the temperature gradient at $x_1 = 0$, there must be a short time interval right after $t = 0$ where temperature diffusion dominates, despite the fact that convection will be the dominant process in the further flow evolution for all Grashof numbers of practical interest. We have conducted trial calculations at various Grashof numbers where the temperature field was initialized with a smooth, but extremely steep interface. During the simulations, both the thickening of the interface due to diffusion and its deformation due to the onset of convection were monitored. These computations revealed that temperature diffusion is clearly dominant for $t < 0.25$, if $\delta \approx 0$ at $t = 0$. As initial condition for the lock-exchange simulations we therefore employed the analytic solution at time $t = 0.25$ of

the pure heat-conduction problem for an infinite channel in which the temperature profile at $t = 0$ is a step function. This analytic solution reads

$$T_0(x_1) = \tfrac{1}{2} - \tfrac{1}{2}\mathrm{erf}(x_1 \sqrt[4]{\mathrm{GrPr}^2}). \tag{54}$$

The number of grid points required to achieve adequate resolution of the initial temperature field depends on the steepness of the profile (54). In our simulations we have used grid sizes in the longitudinal direction of the order of

$$\Delta x_1 \approx (\mathrm{GrPr}^2)^{-(1/4)}, \tag{55}$$

which turned out to be sufficient to achieve a decay of three to four orders of magnitude in the Fourier spectrum of the temperature, not only in the initial stage, but also during the further evolution of the flow. A similarly good resolution is achieved in the velocity field as long as the Prandtl number Pr is not much smaller than one. In the normal direction grid sizes of $\Delta x_3 \approx \Delta x_1$ were used in the interior of the channel, while a much more refined grid was employed in the vicinity of the walls to allow for an adequate resolution of the developing boundary layers.

Since an equidistant mesh is utilized in the longitudinal direction, the length L_1 of the computational domain should be as short as possible in order to minimize the computational costs of the simulations. However, L_1 needs to be long enough to ensure that the frictionless end walls at $x_1 = \pm L_1/2$ exert no significant influence on the propagating fronts. To assess these end-wall influences, we have conducted a number of simulations with identical Grashof and Prandtl numbers, but with widely different channel lengths. A comparison of the results revealed that end-wall influences are essentially confined to a region of width h in the immediate neighborhood of the end walls. Therefore, we have always chosen the box length L_1 such that the propagating fronts were still a distance of at least $2h$ away from $x_1 = \pm L_1/2$ at the end of each simulation.

5.2. SIMULATION RESULTS

To illustrate the typical structure of a lock-exchange flow, Figure 6 shows isocontours of the temperature for different values of the Grashof number. The Prandtl number has been set to $\mathrm{Pr} = 2$ in these simulations. All results in the figure are for the identical non-dimensional time ($t = 14$) after the initial release. For lower Grashof numbers the flow is very diffusive, exhibiting a thick temperature interface in the interior of the channel and only modest gradients at the advancing front. However, even for $\mathrm{Gr} = 2500$ some characteristic features of the head of the front can be observed clearly, for example the existence of a distinct foremost point of the front, the so-called nose, which is raised above the wall. In the low-Grashof-number regime the elevation of this foremost point can be seen to decrease slightly with increasing Grashof number, which is in accordance with experimental observations [1]. The temperature gradients at the head of the front steepen significantly with increasing Gr and require a very fine numerical grid at higher Grashof numbers. For $\mathrm{Gr} = 6{\cdot}125 \cdot 10^5$, for example, a mesh of $N_1 \times N_3 = 512 \times 64$ grid points had to be employed to achieve adequate resolution.

From Figure 6 it is seen that the interface between the heavy and the light fluid is stable at lower Grashof numbers. Kelvin–Helmholtz type instabilities can be seen for the two higher Grashof numbers where patterns of co-rotating vortices emerge. At $\mathrm{Gr} = 6{\cdot}125 \cdot 10^5$ this
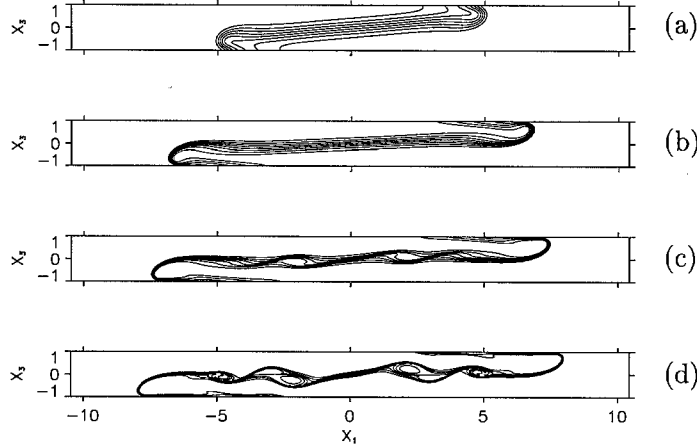
Figure 6. Isocontours of temperature at $t = 14$. Results for different Grashof numbers: (a) Gr $= 2 \cdot 5 \cdot 10^3$, (b) Gr $= 2 \cdot 5 \cdot 10^4$, (c) Gr $= 10^5$ and (d) Gr $= 6 \cdot 125 \cdot 10^5$. Pr $= 2$ and $\alpha_1 = 0 \cdot 15$. Contour lines are evenly distributed between the maximum and minimum values.

interfacial instability is very pronounced. Each of the two progressing currents exhibits one strong vortex immediately behind the head of the front, and a second somewhat distorted vortex further downstream. This second vortex has emerged from two originally separate vortices which have undergone pairing just before $t = 14$. Further pairings do occur in the subsequent evolution of the flow involving new vortices which are continuously shed from the advancing fronts. Note that the simulations are strictly two-dimensional and that, hence, two-dimensional Kelvin–Helmholtz billows may not break up into smaller three-dimensional structures. The pairing will therefore continue until the finite height of the channel inhibits further growth.

In practice, the overall speed at which an intrusion front propagates is of particular interest. If one denotes the (time-dependent) x_1 position of the nose of the front by x_1^n, the propagation speed $\tilde{u}_f$ is given by

$$\tilde{u}_f = \frac{\mathrm{d}x_1^n}{\mathrm{d}t}. \tag{56}$$

The front speed $\tilde{u}_f$ is usually normalized by the buoyancy velocity (5) which gives the Froude number Fr $= \tilde{u}_f / \tilde{u}_b$ of the gravity current [1]. Starting from zero at $t = 0$, the front speed rises rapidly during an initial transient, but attains a fairly constant value after about 5 to 8 dimensionless time units. In order to assess the influence of viscous forces on the propagation velocity of the fronts, we have evaluated this approximately stationary front speed from the results of a series of simulations with different Grashof numbers. We remark that the assessment of such Grashof-number effects is of special importance in DNS. The reason is that in practical applications Grashof numbers are typically very large, whereas direct simulations are constrained to moderate Grashof numbers due to the enormous resolution requirements.

The Grashof-number dependence of the front speed, as obtained from our simulations, is depicted in Figure 7. In the individual simulations very different discretizations were used, ranging from $N_1 \times N_3 = 192 \times 48$ mesh points for the lowest Grashof number (Gr $= 5 \times 10^4$) to 1024×192 nodes for Gr $= 10^8$. It is seen from the Figure that Fr increases significantly with increasing Grashof number over the whole range examined. From theoretical arguments
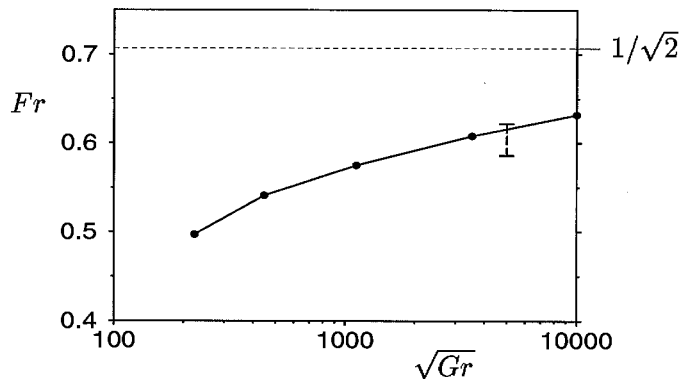
Figure 7. Froude number Fr of the front as a function of Grashof number. Simulations performed with Pr = 1 and $\alpha_1 = 0.225$. $\text{Fr}_{max} = 1/\sqrt{2}$ is the theoretical limit for the Froude number [1]. The vertical bar gives the span of results obtained in lock-exchange experiments with Ar and CO_2 [19].

it is known that an upper limit for the Froude number is $\text{Fr}_{max} = 1/\sqrt{2}$ which can be derived under the assumption that potential energy is converted into kinetic energy without losses [2]. Experimental evidence shows that the high-Grashof-number limit of Fr is only slightly less than this theoretical value and amounts to about 0.65 to 0.67 [1, 9]. Given this and the results shown in Figure 7, we conjecture that the front speed will probably not be independent of Grashof number below $\text{Gr} \approx 10^{10}$.

For comparison, some recent experimental data have been included in Figure 7 and a good agreement between these results and our present simulations can be observed. It should be emphasized, however, that the flow was highly three dimensional in the experiment. The good agreement with our strictly two-dimensional simulations, therefore, suggests that the Froude number of a gravity current is not very sensitive to three-dimensional effects.

Due to both mixing at the interface and friction on the wall, there is a continuous transport of fluid away from the head of a gravity current. In consequence, the internal velocity within the advancing current must be higher than the front speed to provide the mass transport required to balance the occurring losses. In Figure 8 the longitudinal velocity $u_1(x_1)$ is shown for three different time instants of a simulation at $\text{Gr} = 8.15 \times 10^5$ and Pr = 1. The velocities were taken at $x_3 = 0.738$ which is the wall-normal position of the nose of the light-gas front travelling to the right in the upper channel half. The actual position of the front is where the steep increase of u_1 occurs. While for this Grashof number the front speed is about Fr = 0.56 (see Figure 7), much larger values are found for u_1 within the front, as is seen from the three curves. At $t = 10.8$, when the propagating current is fully developed, it is observed that immediately behind the front a zone of constant velocity forms. This constant velocity is approximately 0.65 which amounts to about 1.16 times the front speed. This again is in good agreement with experimentally established results [1, 3].

6. Concluding remarks

In the present paper a numerical method for the direct numerical simulation of lock-exchange flows in a plane channel has been described. Results of a validation study have been presented and a number of two-dimensional simulations of lock-exchange flows have been performed. The simulations are based on the Boussinesq Equations in which density variations
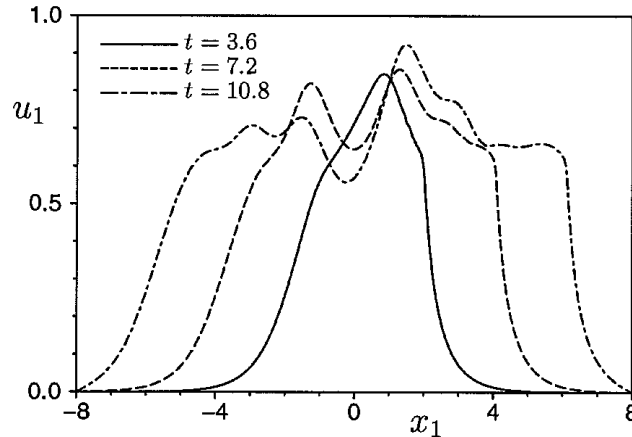
Figure 8. Longitudinal velocity $u_1(x_1)$ at $x_3 = 0.738$ for three different time instants t. Simulation performed with $L_1 = 16$, Gr $= 8.15 \times 10^5$, and Pr $= 1$.

are assumed to be small. For the numerical solution of these equations we apply a mixed spectral/spectral-element discretization in space, coupled with a finite-difference scheme for the time discretization. The algorithm employs a direct solution of the Poisson Equation for the pressure by an influence-matrix technique.

For the validation of the numerical method we have performed simulations of Rayleigh–Bénard convection. From the numerical point of view, the Rayleigh–Bénard flow differs from the lock-exchange problem only with respect to the initial and boundary conditions for the temperature. The results of the Rayleigh–Bénard simulations were compared with linear stability theory and with reference data for steady cellular convection taken from the literature. In all cases an excellent agreement could be observed.

The simulations of two-dimensional lock-exchange flows revealed the typical characteristics of intrusion fronts which have been observed in numerous experimental studies in the past. Among them are the formation of a pronounced head of the front, with a foremost point being raised above the wall, and strong Kelvin–Helmholtz billows which develop at the interface between the light and heavy fluid. The instability of the interface, however, is not observed for smaller Grashof numbers. The propagation speed of the fronts obtained from the simulation results was shown to be in good agreement with recent experimental data. A systematic variation of the Grashof number revealed that the propagation speed is affected by viscosity over the whole range examined. We have estimated that a weak Grashof-number dependence of the front speed may remain up to Grashof numbers of the order of 10^{10}.

The limitations of strictly two-dimensional lock-exchange simulations are illustrated by the fact that the Kelvin–Helmholtz billows at the interface may thicken and pair until the finite width of the channel restrains their further growth. In a three-dimensional situation, however, these large vortices are observed to break up rapidly into small-scale turbulence. In the next stage of our research project we will perform three-dimensional simulations which will allow to analyze this breakup process in detail and to assess its implications for entrainment and mixing at the interface.

7. Acknowledgements

References

1. J.E. Simpson, *Gravity Currents: in the Environment and the Laboratory*. Chichester: Ellis Horwood Limited (1987) 244pp.
2. T.B. Benjamin, Gravity currents and related phenomena. *J. Fluid Mech*. 31 (1968) 209–248.
3. J.E. Simpson and R.E. Britter, The dynamics of the head of a gravity current advancing over a horizontal surface. *J. Fluid Mech*. 94 (1979) 477–495.
4. J.J. Keller and Y.-P. Chyou, On the hydraulic lock-exchange problem. *ZAMP* 42 (1991) 874–910.
5. H.P. Gröbelbauer, T.K. Fannelop and R.E. Britter, The propagation of intrusion fronts of high density ratios. *J. Fluid Mech*. 250 (1993) 669–687.
6. J. Yao and T.S. Lundgren, Experimental investigation of microbursts. *Experiments in Fluids* 21 (1996) 17–25.
7. K.K. Droegemeier and R.B. Wilhelmson, Numerical simulation of thunderstorm outflow dynamics. Part I: Outflow sensitivity experiments and turbulence dynamics. *J. Atmos. Sci*. 44 (1987) 1180–1210.
8. J. Klempp, R. Rotunno and W. Skamarock, On the dynamics of gravity currents in a channel. *J. Fluid Mech*. 269 (1994) 169–198.
9. C.-S. Yih, *Dynamics of Nonhomogeneous Fluids*. New York: The McMillan Company (1965) 306pp.
10. B. Gebhart, Y. Jaluria, R.L. Mahajan and B. Sammakia, *Buoyancy-Induced Flows and Transport*. New York: Hemisphere Publishing Corporation (1979) 971pp.
11. N. Gilbert and L. Kleiser, Turbulence model testing with the aid of direct numerical simulation results. In: *Proc. of the 8th Symposium on Turbulent Shear Flows*. Munich, Sepember 9–11 (1991).
12. Ch. Hirsch, *Numerical Computation of Internal and External Flows, Volume One: Fundamentals of Numerical Discretization*. Chichester: John Wiley and Sons (1988) 515pp.
13. C. Canuto, M.Y. Hussaini, A. Quarteroni and T.A. Zang, *Spectral Methods in Fluid Dynamics*. New York: Springer Verlag (1988) 557pp.
14. G.E. Karniadakis, S.A. Orszag and M. Israeli, High-order splitting methods for the incompressible Navier–Stokes Equations. *J. Comp. Phys*. 97 (1991) 414–443.
15. Y. Maday and A.T. Patera, Spectral element methods for Navier–Stokes Equations. In: A.K. Norr (ed.) *State-of-the-Art Surveys in Computational Mechanics*, New York: ASME (1989) 71–143pp.
16. L. Kleiser and U. Schumann, Spectral simulations of the laminar-turbulent transition process in plane Poiseuille flow. In: R.G. Voigt *et al*. (eds.) *Spectral Methods for Partial Differential Equations*. Philadelphia: SIAM (1984) 141–163pp.
17. P.G. Drazin and W.H. Reid, *Hydrodynamic Stability*. Cambridge: Cambridge University Press (1981) 527pp.
18. R.M. Clever and F.H. Busse, Low-Prandtl-number convection in a layer heated from below. *J. Fluid Mech*. 102 (1981) 61–74.
19. J. Müller and T.K. Fanneløp, Private Communication (1996).